Weierstraß-Institut
für Angewandte Analysis und Stochastik

Leibniz-Institut im Forschungsverbund Berlin e. V.

Preprint ISSN 2198-5855

Fast Raman mapping and in situ TEM observation of metal induced crystallization of amorphous silicon

David Uebel[1], Stefan Kayser[2], Toni Markurt[1], Owen C. Ernst[1], Thomas Teubner[1], Torsten Boeck[1]

submitted: October 6, 2020

[1] Leibnitz-Institut für Kristallzüchtung
Max-Born-Str. 2
12489 Berlin
Germany
E-Mail: david.uebel@ikz-berlin.de
owen.ernst@ikz-berlin.de
toni.markurt@ikz-berlin.de
thomas.teubner@ikz-berlin.de
torsten.boeck@ikz-berlin.de

[2] Weierstrass Institute
Mohrenstr. 39
10117 Berlin
Germany
E-Mail: stefan.kayser@wias-berlin.de

No. 2772
Berlin 2020

2008 *Physics and Astronomy Classification Scheme.* 81.10.−h.

Key words and phrases. Crystal growth, Raman mapping, in situ transmission electron microspcopy, metal-induced crystallization, silicon for photovoltaics .

We thank Andreas Fiedler for countless optimizations to the Raman measurement process and Julian Stöver for his valuable input concerning the data evaluation.

Edited by
Weierstraß-Institut für Angewandte Analysis und Stochastik (WIAS)
Leibniz-Institut im Forschungsverbund Berlin e. V.
Mohrenstraße 39
10117 Berlin
Germany

Fax: +49 30 20372-303
E-Mail: preprint@wias-berlin.de
World Wide Web: http://www.wias-berlin.de/

Fast Raman mapping and in situ TEM observation of metal induced crystallization of amorphous silicon

David Uebel, Stefan Kayser, Toni Markurt, Owen C. Ernst,
Thomas Teubner, Torsten Boeck

Abstract

Crystalline silicon is grown onto an amorphous silicon (a-Si) seed layer from liquid tin solution (steady state liquid phase epitaxy, SSLPE). To investigate the crystallization of embedded a-Si during our process, we adapted Raman measurements for fast mapping, with dwell times of just one second per single measurement. A purposely developed imaging algorithm which performs point-by-point gauss fitting provides adequate visualization of the data. We produced scans of a-Si layers showing crystalline structures formed in the a-Si matrix during processing. Compared to scanning electron microscopy images which reveal merely the topography of the grown layer, new insights are gained into the role of the seed layer by Raman mapping. As part of a series of SSLPE experiments, which were interrupted at various stages of growth, we show that plate-like crystallites grow laterally over the a-Si layer while smaller, randomly orientated crystals arise from the a-Si layer. Results are confirmed by an *in situ* TEM experiment of the metal-induced crystallization. Contrary to presumptions, initially formed surface crystallites do not originate from the seed layer and are irrelevant to the final growth morphology, since they dissolve within minutes due to Ostwald ripening. The a-Si layer crystallizes within minutes as well, and crystallites of the final morphology originate from seeds of this layer.

Introduction

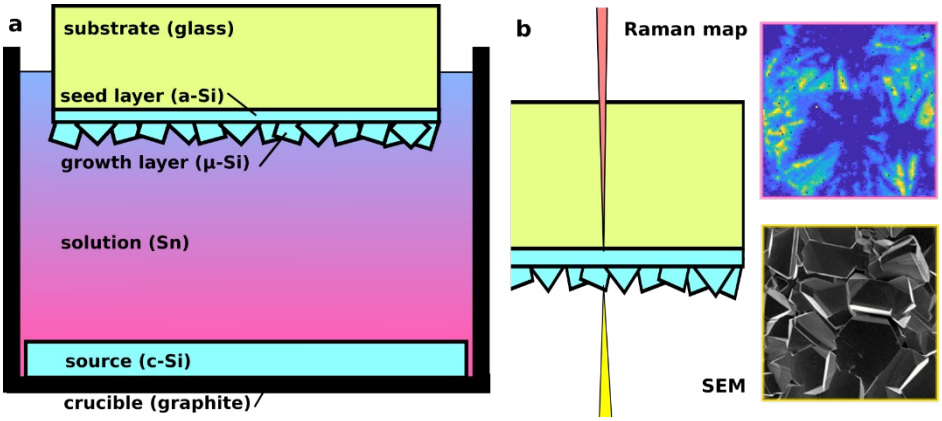

Figure 1 (a) Scheme of the growth crucible build from graphite, including tin solution and a silicon source on the bottom. The substrate temperature is set 5 K colder than the source, so that crystallites grow on the seed layer due to supersaturation of the solution. (b) Visualization of performed measurements: ex-situ characterization of the grown layer from the front side by SEM and from the back side by Raman mapping.

With Steady State Liquid Phase Epitaxy (SSLPE), crystalline silicon can be deposited on amorphous glass. For this purpose a thin amorphous silicon (a-Si) layer serves as seed on a glass substrate. The deposition is performed by solving silicon (Si) in tin (Sn) melt and bringing it to supersaturation. This process is generally known as liquid phase epitaxy (LPE). In the present case, supersaturation is achieved by a temperature difference between Si source and the a-Si/glass substrate stack. The use of a local temperature difference instead of a temperature ramp as with conventional LPE enables the process for continuous deposition. LPE is known for high growth rates and high crystalline quality [1,2], and happens close to thermodynamic equilibrium. These strengths can also be found within the SSLPE procedure. The crucial factor is that SSLPE can also be used for amorphous substrates, and non-conventional crystalline substrates [3]. The deposition of Si for example is already possible at temperatures of 500 °C, whereas conventional Si processing requires high temperatures above the Si melting point of 1414 °C. Thus the SSLPE process is not only more flexible, but also consumes less energy. The flexibility in substrate choice, the very low process temperature and the Sn float bath enables for example the production of large silicon sheets on glass with areas well over 1 m². These large Si sheets are needed for the production of solar modules.

Despite progress in alternative semiconductor materials for photovoltaics, crystalline silicon still makes up for the majority of the photovoltaic market. Unlike its competing solar materials, silicon is abundant in the earth's crust, easily accessible, non-toxic and well understood. Commercial cell designs can achieve average efficiencies of 22.8 % (multi-crystalline Si) and 26.1 % (mono-crystalline

DOI: 10.20347/WIAS.PREPRINT.2772 Berlin 2020

Si) with further progress every year [4]. The largest cost factor of a silicon solar cell is the absorber material. Its production, including refining, rod or block production, wafering, and material loss during surface preparation accounts for 25 % of the total cell costs [5]. Reduction of the invested material is a great opportunity to save costs, but the prospect of a further reduction of the invested silicon is diminishing [6]. A state-of-the-art absorber has a thickness of 180 µm, of which just 50 µm are required for the absorption of sun light. The additional 130 µm of Si is needed for mechanical stability during sawing and to keep the wafer mechanically intact during processing. Further thinning would mean a direct cost reduction, but there are reports that strongly question the possibility of industrially reducing the thickness further than 150 µm, as bending such thin layers quickly introduces numerous dislocations and would therefore greatly reduce the life of the substrates during manufacture. Further thinning would mean a direct cost reduction, but there are reports which decidedly question the possibility to industrially lower the thickness further than 150 µm [6,7,8]. An alternative to bulk production are thin Si films on cost-efficient substrates. The major challenge here is to produce layers thick enough for light absorption and of adequate crystal quality. We have developed a method to grow a polycrystalline layer on glass. The glass substrate guarantees the mechanical stability, and the silicon is produced in a compatible way to thin-film techniques. With our SSLPE approach, we can grow silicon up to a thickness of 50 µm without waste of raw material. Si crystallites grown by this method show a significantly low dislocation density and promising electrical properties [3,9]. Also elemental contaminations are well within the specifications of solar grade Si [9]. Previously performed Raman and photoluminescence measurement revealed high crystal grade and no internal stress [9]. Ongoing electrical characterization reveals promising lifetimes and no compromising deep level defects in the crystal material, which have been excluded here due to the scope of this publication. For production of Si sheets on glass for photovoltaic applications by SSLPE growth, an amorphous silicon (a-Si) seed-layer is prepared by physical vapor deposition (PVD). Subsequently, this sample is inserted into a liquid tin (Sn) bath supersaturated with Si at the interface between sample and bath. Crystalline Si (c-Si) now grows on the seed layer. The influence of the seed layer during growth was observed in earlier experiments [9,10], but the detailed mechanism of c-Si growth on the a-Si layer was not yet revealed. In previous work we have found that several experimental conditions have to be considered more closely. Examples are the content of reactive species such as water and oxygen either in the ambient atmosphere or in high vacuum or the control of Sn bath saturation by Si at the beginning of growth. It is known that a-Si does not need to be molten for crystallization, but undergoes the phase transition from amorphous to crystalline when exposed to temperatures far below its melting point. During this process, higher temperatures lead to shorter incubation times and to faster crystallization rates [11]. The final morphology also depends strongly on the Si deposition parameters [12]. The exposure to metal layers like Sn promotes the

crystallization as well. This is referred to as metal-induced crystallization (MIC): Atoms of the a-Si layer in contact to a Sn layer will diffuse through the grain boundaries of the Sn due to the increased defect density there. Additionally, the formation energy for silicon grains is lowered by the neighboring Sn crystals [13]. The combination of both effects leads initially to rapid nuclei formation and further to an enhanced growth rate of silicon crystals. Since they form in the Sn matrix, MIC may lead to a layer transfer of the precursor layers of Sn and Si [13]. Originally the formation of a liquid mixing phase of Si and Sn was expected to be the reason for fast c-Si formation. The liquid solution would act as fast diffusion medium and would also produce dangling bonds on the surface. *In situ* MIC experiments disproved the theory that a liquid phase formation takes place. [13]

For the process presented here, a-Si is used as precursor layer and Sn is used as diffusion medium as well. Contrary to the case described above, the Sn is liquid and not crystalline and thus making reports for MIC in the presented system not fully applicable. Examples of liquid metal acting as a catalyst for amorphous material do exist, but are not fully understood, unlike the MIC process [14]. The central detriment is the absence of Sn crystals and thus Sn crystal boundaries, which would otherwise act as nucleation sites during MIC. However, the large volume of liquid solution as diffusion medium here should cause faster diffusion, opposed to the small diffusive volume of grain boundaries during MIC. Former experiments [11] have shown nano-crystalline sites in the a-Si layer which act as nuclei during growth, so as for MIC, nucleation sites with a higher crystallization probability exist within the material system. It is reported [15] that liquid Sn droplets act as propagation sites, from which c-Si dendrites grow into the matrix.

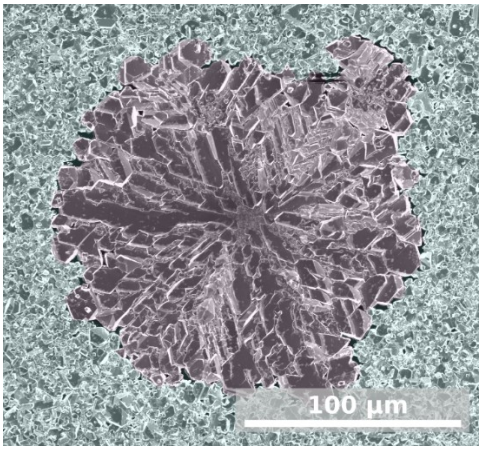

Figure 2 *growth morphology of a plate-like rosebud of coordinated large crystallites embedded in stochastically orientated smaller crystallites. Hand-colorized to indicate plate-like (magenta) and stochastic (teal) morphology.*

Studying morphology phenomena of SSLPE layers, bimodal growth can be observed (figure 2). The morphology shown here has been of interest for some time, but its origin could never be identified. Normally SSLPE exhibits stochastic crystallite orientation and gravel-like surface coverage (as shown as teal in figure 2). Figure 2 also shows a rarer morphology of round, plate-like crystals, which exhibit

a coordinated (111) preference. Understanding how two completely different morphologies coexist is the key to a holistic growth model of SSLPE. To identify and trace back the growth phenomena's origin, we interrupted the growth process of identical a-Si samples at different stages and observed the surface of the grown c-Si layer by scanning electron microscopy (SEM) and the seed layer by Raman mapping from the back through the glass substrate. Especially Raman mapping as used here, is a flexible, fast and non-destructive method to make crystalline phases in the seed-layer visible. We adapted the mapping workflow extensively. As established in this paper, it considers the unique sample geometry and uses data post-processing to enable impromptu morphology monitoring. The catalytic effect of Sn on a-Si is described in literature, but just for the reaction with crystalline Sn [11–13]. To gain a direct insight into the interaction and to underline the results of Raman mapping, an *in situ* TEM experiment was designed to observe the reaction.

Experimental

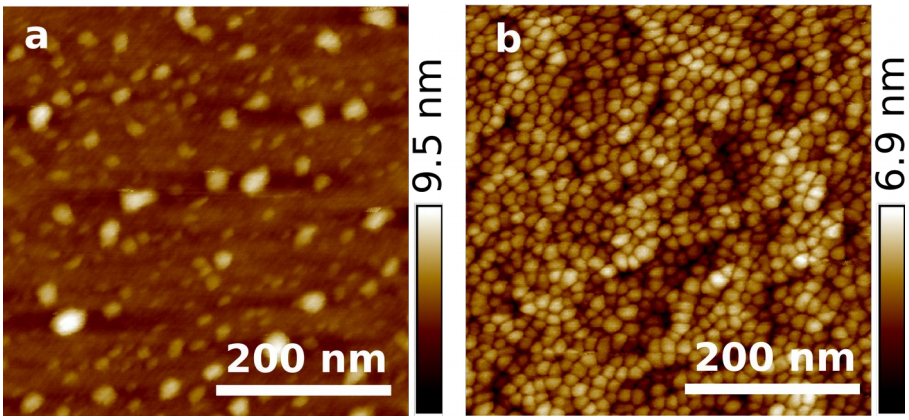

Figure 3 AFM scan of the substrate glass with a roughness of R_q = 41.3 nm (a) and the a-Si seed layer with a roughness of R_q = 74.35 nm (b)

The preparation of the final absorber layer involves three steps: seed layer preparation, oxide removal, and Si growth from Sn solution. In the first step, a-Si seed-layers are prepared by PVD on Corning® EAGLE XG® glass of 0.9 mm thickness and a roughness of R_q = 41.3 nm. For this purpose, the front side of the glass substrate is heated to 400 °C with heater lamps. Si is then evaporated to a final thickness of 2 µm using an electron beam with 8 kV at currents between 150 and 210 mA, resulting in growth rates around 1.6 nm·s^{-1}. Layer thickness is reliably measured in situ by and oscillating quartz and confirmed with profilometry on a regular basis. The final roughness of the substrate results in R_q = 74.35 nm (figure 3). To reduce the influence of variations during PVD on single process runs, 8 samples are prepared simultaneously during one evaporation run. These samples are then stored between a day and several weeks. Our experiments show that with adequate HF-dipping, experiments are repeatable with very reliable growth results, independently from storage time. For each growth experiment, a single sample is dipped in freshly prepared 4 % hydrofluoric acid solution

for 20 s and afterwards rinsed in de-ionized water to establish an H-termination. Hydrofluoric acid is highly poisonous and corrosive. Its ability to penetrate many materials require the operator to take special safety percussions accordingly. The sample with the passivated a-Si layer [16] is then transferred within minutes into the growth chamber filled with pure H_2 at ambient pressure, since the re-oxidation can happen in short periods of time, especially for a-Si with its high density of surface states [17]. The growth is achieved by placing the substrate in a crucible which contains a silicon source fixed on its bottom with liquid Sn above (Figure 1a). The Sn at the Si source at a temperature of 605 °C can solve $0.346 \cdot 10^{-3}$ at-% Si, which supersaturates Sn near the substrate surface that is held at 600 °C which solves just $0.31 \cdot 10^{-3}$ at-% Si [18]. Consequently nucleation and subsequent growth of silicon crystallites takes place.

A series of experiments varying the growth duration from 1 s to 1 h on otherwise identical a-Si samples was carried out, so that crystal morphologies at consecutive growth stages could be

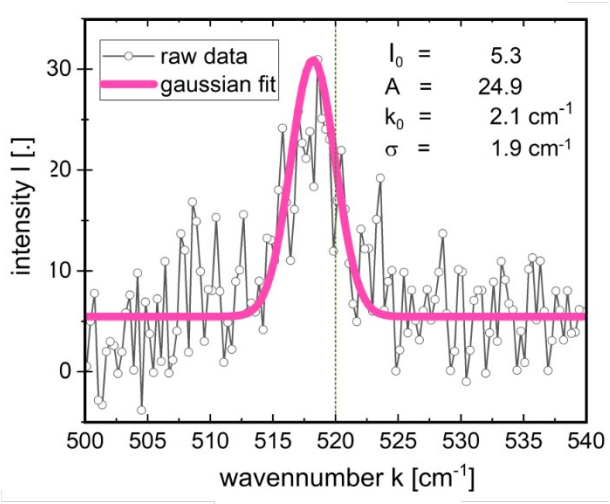

evaluated and compared.

Figure 4 *Raman signal of an individual measuring point and demonstration of the Gaussian fit in the form of*

$$f(x) = I_0 + A \cdot \exp\left(\frac{-1}{2}\left(\frac{k_{cr} - k_0}{\sigma}\right)^2\right)$$

with I_0 – offset, A – maximum peak height, σ - standard deviation from bulk Si signal, and x_0 – peak center deviation from k_{cr} . The peak of the multi-crystalline c-Si k_{cr} layer shows a downshift due to the small crystal sizes compared to bulk Si (dotted line at 520 cm^{-1}).

For the primary understanding of the morphology of the growth layer, scanning electron microscopy was performed from the front side of the grown layer. Raman maps of the seed layer were obtained

by scanning the areas of interest from the back by a 100 × 100 pattern. Raman maps from the front could not be obtained. The SSLPE layer is too rough for automated mapping and would require continuous refocusing. The seed layer would lie behind several 10 µm of c-Si, which absorbs the used laser light with 1 µm. Contrary to Gouadec et al. [19] we modified the mapping procedure as follows: To keep process time low, a 633 nm He-Ne laser was focused with a 100 × magnifying near-infrared lens with a focal distance of 4.7 mm. The large focal distance allows to measure through the substrate glass. The high magnification of the lens is necessary to reach low dwell times. Since a temperature-dependent amorphous-to-crystalline reaction is observed, temperature damage to the samples are a concern with high-focusing lenses. Simulations with COMSOL Multiphysics® according to models presented in literature [20] show that the laser pulse will only cause temperature to increase a few Kelvin and thus will not damage the amorphous silicon. The signal-to-noise ratio is improved by the confocal setup of the spectrometer, which collects signal primarily from the focal point of the exciting laser. With the described setup we were able to reduce the dwell times for each measurement point to as little as 1 s and still obtain image information that is sufficient for a well specifiable contrast. Usually, Raman spectra of c-Si in a-Si matrices are fitted with two or more Gaussians to accommodate for the amorphous phase, for multiple Raman modes, and for asymmetry in the peaks [21,22,23,24]. Due to high noise ratio in the fast measurements, we decided to use only one Gaussian (figure 2) fit in the form of

$$I(x) = I_0 + A \cdot \exp\left(\frac{-1}{2}\left(\frac{k_{cr} - k_0}{\sigma}\right)^2\right),$$

where A corresponds to the peak height, x_0 to the peak deviation from the characteristic peak k_{cr} of c-Si at 520 cm^{-1}, and σ to the standard deviation. The a-Si signal is weak and does not contribute to the recorded spectra (figure 6a). For the mapping itself, to accommodate not only for peak intensity A but also for its standard deviation σ, a quality coefficient A/σ was introduced. As we will describe later, combining the two increases structure information obtained. Software package MATLAB® R2018a was used to fit and plot the data.

Complementary to the series of interrupted growth experiments, an *in situ* TEM experiment was carried out to visualize the reaction between Sn and a-Si. A comparable *in situ* vapor-liquid-solid (VLS) experiment for the precipitation of GaAs from GaAs solution has been demonstrated by Harmand et al. [25]. For the *in situ* observation of our process, a Sn layer of several hundred nm was deposited on the above described a-Si layer by thermal evaporation. A cross-sectional TEM sample has been prepared of the stack consisting of glass, a-Si and Sn. The stack prepared so that all interfaces are in the field of view and thus both etching and crystallization of the a-Si would be visible (Figure 6a), as well as the Si precipitation within Sn. This was achieved by HF-dipping a glass/a-Si

substrate and inserting it into the PVD chamber in a vacuum of $5 \cdot 10^{-6}$ mbar. Sn was deposited by resistance evaporation and accordingly low deposition rates. Due to long deposition time of several hours and the heat from the heater crucible we expect a SiO_X to regrow. The sample was prepared by plan parallel mechanical polishing down to a thickness of 10 µm followed by Ar^+-ion milling in a PIPS Gatan Inc. system with liquid N_2 cooling, then extracted by Focused Ion Beam (FIB) with the FEI Nova 600 NanoLab DualBeam™ SEM/FIB, and finally mounted on a Fusion Select heating cell of Protochips, Inc (Figure 6b). To prevent charging of the sample during FIB-extraction. Figure 6b shows the prepared lamella mounted onto the heater chip. The TEM experiment was performed in a FEI Titan® 80-300 TEM/STEM.

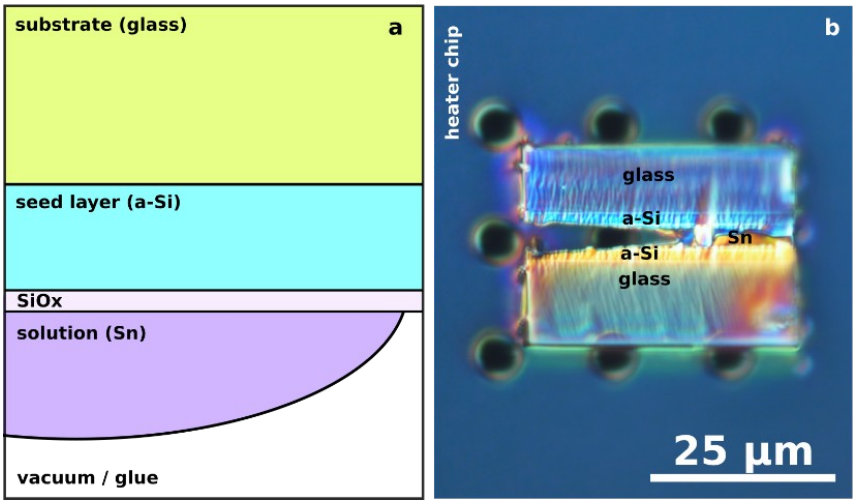

Figure 5 scheme (a) and light microscopic image (b) of the cross-sectional TEM specimen prepared for in situ observation of metal induced crystallization of a-Si. The stack was prepared by PVD evaporation of Sn onto an existing a-Si seed layer followed by the TEM-preparation. The In (b), the lamella cut by FIB is placed on the in situ TEM heating chip with the region of interest placed above holes in the heating chip.

Results

Raman spectroscopy

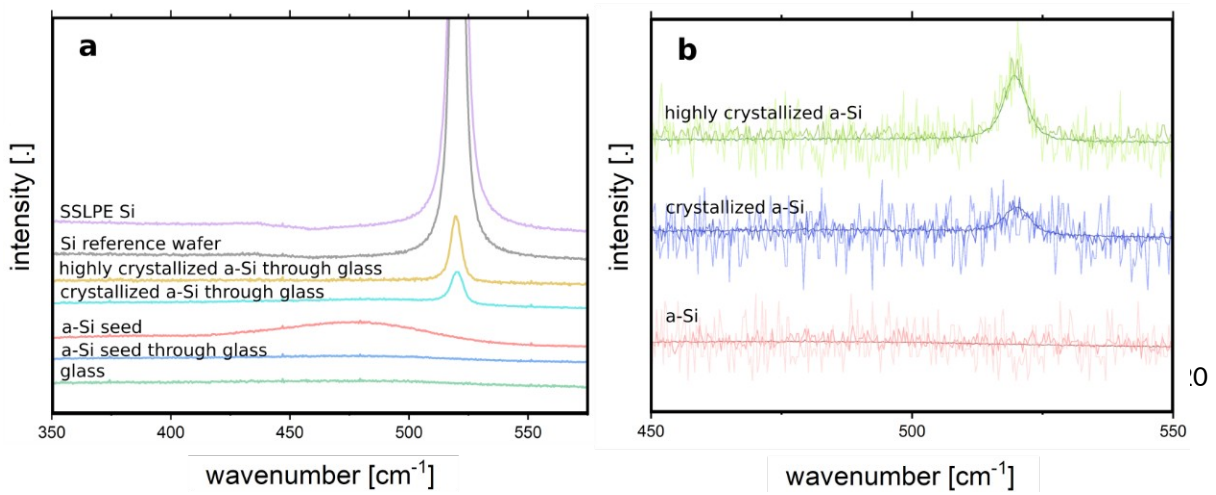

Figure 6 *(a) Raman spectra of various Raman signals connected to the experiments shown. SSLPE c-Si is identical to commercial wafer Si with a strong refined peak at 520 cm^{-1}. The seed layer has to be measured through glass and thus shows high reduction in intensity. Amorphous Si shows a broad band around 480 cm^{-1} and becomes nearly flat when measured through glass. Crystallized a-Si is embedded between the SSLPE growth layer and glass and can only be measured through the latter. Its signal is weak, even for the most annealed states observed. All measurements are recorded with 8 min of dwell time. (b) visualizes how shorter dwell times influence the signal-to-noise ratio. All signals are measured on the backside of the silicon layers through the glass substrate. Darkest lines represent 8 min, lighter ones 5 s and the lightest 1 s. A dwell time of 1 s was used for mapping. Only the rare highly crystallized states are easily recognizable, but most states of interest are within the blue plot. For these states, noise is larger than the crystalline signal*

Figure 7 shows the various material occurrences and the different Raman spectra used for this work. As visible in figure 7a, SSLPE c-Si is not distinguishable from a commercial Si wafer. Both show a sharp peak at 520 cm^{-1}. The a-Si seed layer shows a broad peak around 480 cm^{-1}. Since SSLPE crystallites form on it during growth, its crystallization reaction can only be observed on the backside through substrate glass. The Raman a-Si signal then is flat and indistinguishable from glass. Crystallized seed is observable but shows smaller peaks which show a blue-shift (compare figure 5). Figure 7b visualizes signal degeneration when going from 8 min of measurement time to 1 s and both times measuring through glass. Especially the intermediate signal (blue lines) shows how noise can surmount signal. For the phenomena observed, differentiation is most important in the range of the intermediate signal (blue) and the amorphous signal (red). Gauss fitting (figure 4) is able to extract useful information from 1 s measurements through glass.

Figure 7 shows how the point measurements of one Raman map develop from the first map at 1 s to the last map at 1 h (the spreads refer to the maps shown in figure 9a-1 and figure 9a-6). In figure 7a, most of the obtained central wave numbers show a blueshift of at least 1 cm^{-1} up to 6 cm^{-1}. A number of Raman peaks show broadening up to a standard deviation of 5 cm^{-1}. As shown by the red line, broad peaks also show more blueshift. The highly crystallized state in figure 7b shows generally less peak deviation and less broadening. Amorphous and crystalline phases of the same chemical composition show very different Raman spectra. Raman shift is dependent on the relative movement of atoms. The amorphous signal is dominated by short-range order and thus its point group, while the crystalline one is dominated by long-range order and thus its space group [26]. Figure 7 shows different positions of the center of the peak values between early and late stages of crystallization. Silicon crystallites smaller than 10 nm show a downshift in that value. The early stage shows broader peaks (higher σ values), since smaller crystallites exhibit lattice expansion and lattice functions are not fully developed [21,24].

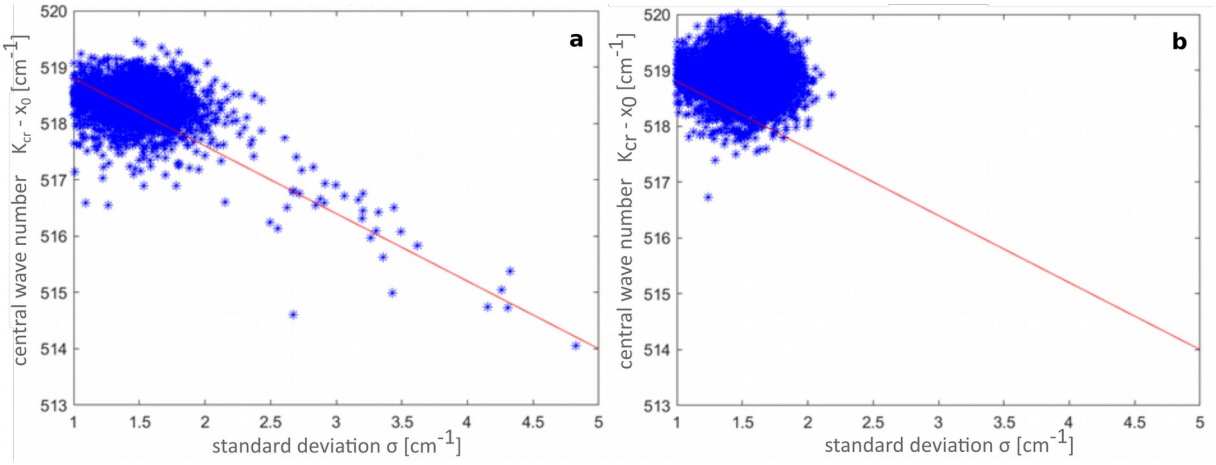

Figure 7 *spread of all measurement points with a standard deviation σ larger than 1 cm^{-1} after 1 s of growth (a) and after 1 h (b). A downshift in central wave number x_0 is correlated to broader Raman peaks. The crystallized seed layer in plot b only shows peaks between 518 and 520 cm^{-1}, while the initial state shows Raman shifts down to 514 cm^{-1}. Red line serves as guide to the eye.*

Surface morphology succession during growth (SEM)

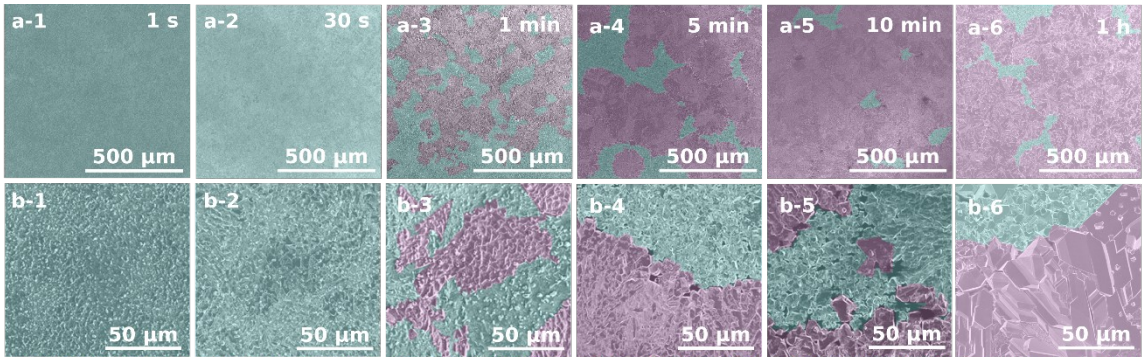

Figure 8 colored *SEM images of different stages of surface morphologies during growth – overview in the upper row, characteristic features with higher magnification in the lower row. (a/b-1 to 3): Immediately after growth starts, crystallites on the surface are visible (colored teal). Initial crystallites are close-grained and randomly orientated. (a/b-4 to 6): A second growth morphology appears, more bulky and tile-like than the initial one (colored magenta). Initial close-grained crystallites grow in volume, but decrease in number.*

The SEM imaging of the surface (figure 8) shows two distinct growth modes, active during different stages of the growth. At 1 s, a high number of crystallites is visible on the surface. They are closely grained and randomly orientated. Up to the period of 1 min, the number of visible surface crystallites decreases, while their size increases.

From 1 min on, larger and tile-like crystallites are visible and are recognizable throughout the growth. Early in their development, they appear in clusters of separated chunks. Later they join together to form large, round plates with diameters of about 150 µm. Facets of the involved crystals point to the center of the circles. The plates are sometimes separated, but mostly interconnecting and spanning large areas. Even in large aggregations of these plates, lines on facets still cross in centers of recognizable circles.

Seed layer morphology during growth

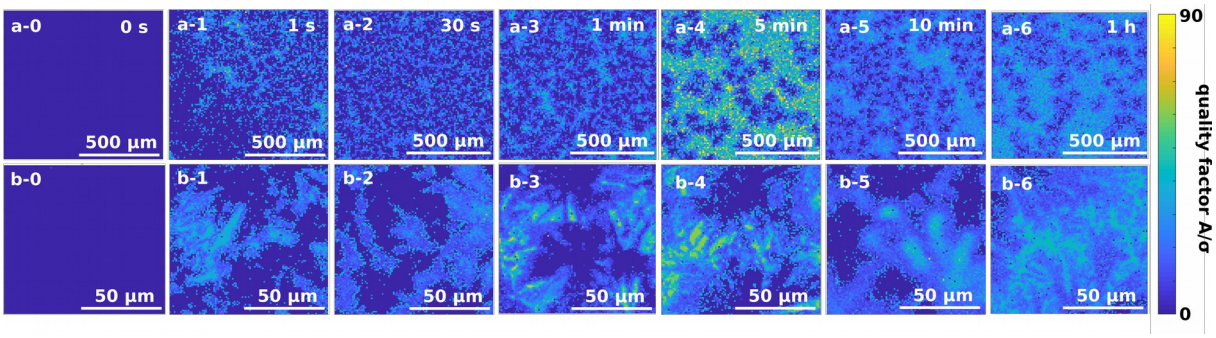

Figure 9 Raman mapping of the crystallite's peak of c-Si at 520 cm-1 represented by a quality factor A/σ. Overview in the upper row, characteristic features with higher magnification in the lower row. 1st stage: The amorphous silicon matrix crystallizes from seeds, forming dendrites which coalesce into networks (a-1 to 2). 2nd stage: Crystalline dendrites become thicker, as well as more refined, making the former matrix now invert and embedded in crystalline material (a -3 and 4). 3rd stage: the morphology is conserved (a-5 and 6). (a/b-0) shows the initial, fully amorphous state of the seed before growth.

Figure 9 shows the mapping of the quality factor A/σ. Amorphous and crystalline phases of the same chemical composition show very different Raman spectra. Raman shift is dependent on the relative movement of atoms. The amorphous signal is dominated by short-range order and thus its point group, while the crystalline one is dominated by long-range order and thus its space group [26]. Figure 4 shows different positions of the center of the peak values between early and late stages of crystallization. Silicon crystallites smaller than 10 nm show a downshift in that value. The early stage shows broader peaks (higher σ values), since smaller crystallites exhibit lattice expansion and lattice functions are not fully developed [21,24]. In the final stage of growth, amorphous islands are no longer recognizable and the seed layer completely consists of crystalline material. Even if all material in an area appears to be crystalline, there is varying signal over the area.

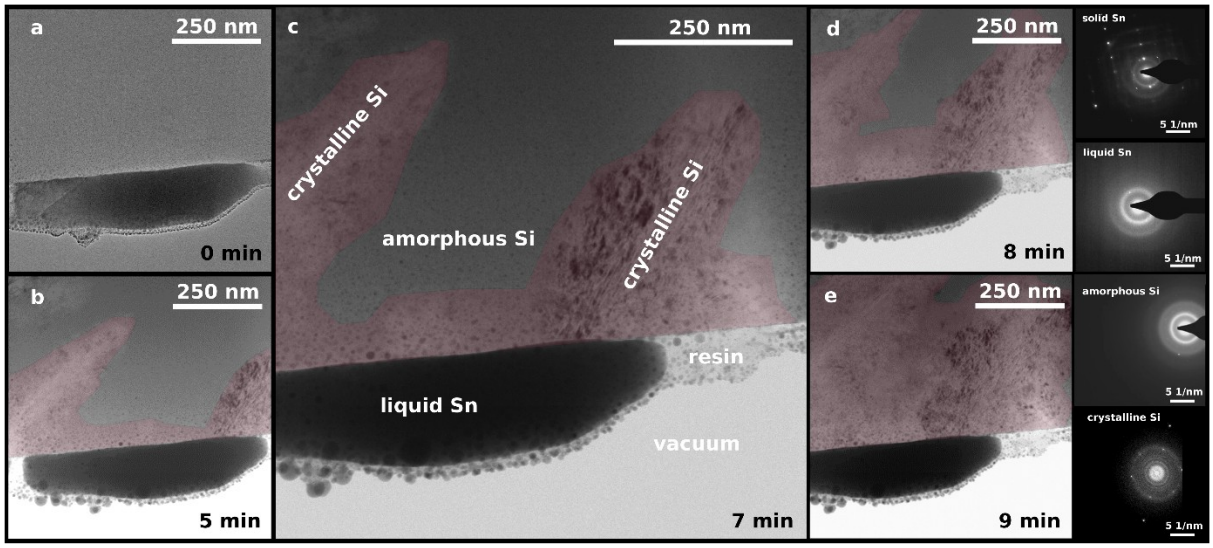

Figure 10 *TEM succession of a crystalline seed evolving from the contact point of a-Si and liquid Sn. Images are taken in bright field mode with reduced aperture to provide high sensor exposure with crystallite contrast which can detect different lattice angles. Crystallized Si is colored red manually (a) shows the stack before process temperature is applied, (b) to (e) show ongoing crystallization at 600 °C.*

The *in situ* TEM experiment (Figure 5) was modelled after the conditions at the beginning of the growth. Due to technical factors, it was not possible to deposit Sn on Si without a SiO_x layer in between and the initial Sn-droplet was not (super-)saturated with Si. Nevertheless the *in situ* model is in good agreement with findings already presented in this work. Crystallization starts after an incubation time of 5 min at the interface of Sn melt and a-Si (10b). The crystallization itself progresses over another 5 min. Figure 10 shows a dendrite with a diameter of 250 nm grow into the a-Si matrix. The interface line of Sn and Si does not change during the experiment, nor does it indicate etching. Nevertheless shrinking of the Sn droplet is observed.

Discussion

On the sample surface different crystal growth modes emerge during the growth. Early small crystallites (surface crystallites, Figure 8b-1 and 2) are followed by plate like crystallites (Figure 8b-3 and later) and finally large, interconnected crystallites (Figure 8b-6) form. Surface crystallites spawn in large numbers immediately as growth starts, which stem from an oversaturation of the melt in the moment of sample dip-in. This is supported by the TEM investigation, were no Si-precipitation within the Sn melt occurs. The Sn phase is not supersaturated in the TEM experiment. An explanation for supersaturation could be a slight undercooling. The sample in waiting position for dip-in might not be completely adjusted to solution temperature. When inserted, the colder sample surface causes high supersaturation which leads to an immediate crystallization of a high number of nuclei. An alternative explanation is the prior supersaturation of the Sn melt. This could happen since the Sn surface is set to growth temperature before contact with the substrate. Silicon atoms solved at the hotter source would defuse there and again cause supersaturation. Theses phenomena are not observed in the TEM experiment. That's only coherent: the small volume of material should not exhibit temperature differences within the observed volume and thus no supercooling. From figures 8b-1 to b-4, the development of surface crystallites is observed. The crystallites decrease in number while increasing in size and as already described is an effect known as Ostwald ripening [27]. Ostwald ripening is caused by the difference in surface pressure of droplets and particles. Smaller droplets and particles interconnected to larger droplets by a diffusion enabling medium will decrease in volume and eventually disappear in favor of the larger droplets. In material science, Ostwald ripening is widely used to explain morphology changes of bulk material, for example during heat treatment of construction alloys[28,29]. Hereby, smaller crystallites also shrink in favor of larger crystallites, in a solid-solid reaction of the particles. We think that this model is applicable here as well, since crystallites on the surface can exchange material quickly through the melt. Plate like crystallites are observed primarily between Figure 7b-4 and b-6, with early forms conceivable already in Figure 8b-2. As described above, these crystals appear to share orientation, so they should originate from the DOI:

same source. Between Figure 7b-4 and b-6, additionally to plate-like crystallites, a rough surface characterized by small crystals is observed.

These observations give now the ability to explain the growth morphology phenomenon in question. The correspondence of the two coexisting morphologies is clarified by comparison of the microstructure of the growth layer and the seed layer. The seed layer shows bimodal coexistence of amorphous and crystalline phases. The shape of the amorphous islands resembles the shape of the plate-like structures (compare Figures 8 and 9 within the respective b-4 to b-6). We think that plate-like structures come to existence because they can grow over an area which is not crystallized. In areas with crystallized seed layer, lateral overgrowth seems to be impossible. Instead, the Sn melt crystallizes this area. In contrast, amorphous seed-layer areas appear to be protected from the reactions caused by Sn. Figure 10 shows a Si crystallite growing vertically into a-Si. Crystallites with this behavior would be promptly observed in Raman mapping when they grow towards the glass interface, since the Laser is focused on the interface. Additionally, a-Si absorbs 633 nm light fast (absorption coefficient $\alpha = 10^{-4}$ cm^{-1}) [30]. Laterally growing crystals would not come close to the interface and would not be observed. Plate like crystallites may stem from lateral expansion which grow epitaxially as presented in figure 2. The crystallization is catalyzed by Sn (figure 10) and the crystallites form a contact barrier between Sn and a-Si, hindering a further reaction and conserving a-Si. When nuclei grow vertically, the surface area they span is smaller, leaving space for additional nuclei to form. Vertical nuclei grow towards the interface plane of a-Si and glass. Raman measurements are performed at that interface and will be observed by Raman mapping. Since vertical crystallites protect underlying a-Si from Sn induced crystallization it will crystallize slow and not much change is observed in already formed amorphous islands (compare figure 9 b-3 and 4). On the contrary surface crystallites will grow thicker and thus change appearance (figure 8 b-3 and 4).

Twinning observed in SEM indicates that surface energies of the evolving crystallites changed during growth. During solution growth crystallites grow near the thermodynamic equilibrium and should not show twinning. Since the growth temperature did not change during the experiments, we expect the facets to reach critical sizes which change the preferred growth mode slightly.

TEM and Raman observations offer conforming insights into seed layer crystallization despite revealing a number of differences. When considering the characteristics of the experiments, different results are explained by the differences in the set-up. The considerably higher measured incubation time in the *in situ* TEM experiment, which is in contrast to the immediate crystallization in the growth experiment, could be explained by a reduced real temperature of the studied part of the in situ TEM lamella compared to the nominal temperature of 600°C of the heating chip to which the lamella is attached to. This difference in turn is plausible because of the limited thermal contact between

heating chip and the lamella and the limited heat transport within the thin platelet-like lamella. Also, Sn is separated from a-Si by a SiO_x layer, which should hinder a reaction initially. However, incubation time in a-Si without metal catalyst at a temperature of 600 °C has been reported at 30 h [8]. Both the Raman mapping and the TEM show drastically quicker crystallization, with liquid Sn acting as a catalyst. Both methods reveal dendritic growth of crystallites.

Raman spectroscopy shows the high crystal perfection of SSLPE crystals, with its Raman signal basically indistinguishable from the one of a commercial wafer (figure 7). This is promising for photovoltaic application. This is not true for the nuclei in the crystallized seed. We expect solar cells manufactured from this material suffering from the influence of the high density of small nuclei with softer Raman brilliancy (figure 5 and 7), referring to higher density of lattice defects or even lattices which are not fully developed. The described morphology of plate-shaped crystals with amorphous material underneath might be a helpful option. By conserving a-Si less nanocrystalline material would introduce recombination sites. . Also these crystals are larger and thus exhibiting less grain boundaries which is also a perspective for improvement. Additionally the alternative sample surface geometry could achieve better surface coverage and might be better to process.

Conclusions

An unexplained morphology phenomenon of plate-like crystal structures was investigated with different methods. Well-known methods such as TEM and Raman mapping were adapted purposefully to investigate different sample parts in a destruction free manner. By studying interrupted growth experiments from identical seed layers, we were able to show a new and much more detailed model of the presented c-Si layer growth method. We identified different growth modes during the 1 h of growth. From the different growth modes presented by the intermediate morphologies, we showed that not all contribute directly to the final morphology. Originally the initial surface crystallites were thought to be the origin of the crystals which form the final layer. Our experiments show that initial crystallites disappear within the growth driven by Ostwald ripening. By an *in situ* TEM experiment, we demonstrated that the nucleation of these surface crystallites originates from the supersaturation of the Sn melt in the moment of the exposure to an a-Si surface. Crystallization of the seed layer happens dynamically within the first minutes of growth, supported by the contact to the melt. A fast Raman mapping procedure to capture the phase development within the seed layer was applied. We presented a network of crystalline dendrites growing into the a-Si matrix. Dendrites enlarge and eventually a matrix inversion is observed, only leaving residue of amorphous islands within a crystalline matrix. A surface feature of plate-like crystals is observed exclusively on these islands. The results show an unreported connection of seed and growth layer

and allow new paths of optimization. The presented mapping workflow is robust and suitable of extremely low Raman measurement times. The ability to detect the slightest change in the various properties of a highly noisy Raman peak makes it a promising method for other material systems.

Reference:

1 J. McNeely, R. B. B. Hall and W. A. Tiller, *J. Cryst. Growth*, 1984, **70**, 420–426.

2 B. J. Baliga, *J. Electrochem. Soc.*, 1986, **133**, 5C-14C.

3 C. Ehlers, R. Bansen, T. Markurt, D. Uebel, T. Teubner and T. Boeck, *J. Cryst. Growth*, 2017, **468**, 268–271.

4 NREL, Best Research-Cell Efficiency Chart, https://www.nrel.gov/pv/cell-efficiency.html, (accessed 11 December 2019).

5 VDMA Photovoltaic Equipment, *ITRPV*, 2019, 9.

6 J. Kroon, *Cheetah - Project Final Report*, 2017.

7 H. Sivaramakrishnan Radhakrishnan, J. Cho, T. Bearda, J. Röth, V. Depauw, K. Van Nieuwenhuysen, I. Gordon, J. Szlufcik and J. Poortmans, *Sol. Energy Mater. Sol. Cells*, 2019, **203**, 110108.

8 J. Kroon, P. Sommeling, M. Schmid, S. Gevorgyan and M. Heisz, *D5.4 – Final report on the R&D impact on cost reduction*, 2018.

9 R. Bansen, R. Heimburger, J. Schmidtbauer, T. Teubner, T. Markurt, C. Ehlers and T. Boeck, *Appl. Phys. A Mater. Sci. Process.*, 2015, **119**, 1577–1586.

10 R. Bansen, C. Ehlers, T. Teubner, T. Markurt, J. Schmidtbauer and T. Boeck, *CrystEngComm*, 2016, **18**, 1911–1917.

11 R. B. Bergmann, G. Oswald, M. Albrecht and J. Werner, *Solid State Phenom.*, 1996, **51–52**, 515–520.

12 R. B. Bergmann, G. Oswald, M. Albrecht and V. Gross, *Sol. Energy Mater. Sol. Cells*, 1997, **46**, 147–155.

13 Z. Wang, L. P. H. Jeurgens and E. J. Mittemeijer, in *Metal-Induced-Crystallization*

Fundamentals-and-Applications, eds. Z. Wang, L. P. H. Jeurgens and E. J. Mittemeijer, Pan Stanford Publishing, 1st edn., 2015, pp. 25–55.

14 R. Heimburger, N. Deßmann, T. Teubner, H. P. Schramm, T. Boeck and R. Fornari, *Thin Solid Films*, 2012, **520**, 1784–1788.

15 V. Neimash, V. Poroshin, P. Shepeliavyi, V. Yukhymchuk, V. Melnyk, A. Kuzmich, V. Makara and A. O. Goushcha, *J. Appl. Phys.*, , DOI:10.1063/1.4837661.

16 G. W. Trucks, K. Raghavachari, G. S. Higashi and Y. J. Chabal, *Phys. Rev. Lett.*, 1990, **65**, 4.

17 H. Angermann, W. Henrion, M. Rebien and A. Röseler, *Solid State Phenom.*, 2003, **92**, 179–182.

18 R. Bansen, Humboldt-Universität zu Berlin, 2016.

19 G. Gouadec, L. Bellot-gurlet, D. Baron, P. Colomban, G. Gouadec, L. Bellot-gurlet, D. Baron, P. Colomban, G. Gouadec, D. Baron and P. Colomban, in *Raman Imaging*, ed. A. Zoubir, Springer, Berlin, Heidelberg, 2018, pp. 85–111.

20 C. Ehlers, S. Kayser, D. Uebel, R. Bansen, T. Markurt, T. Teubner, K. Hinrichs, O. Ernst and T. Boeck, *CrystEngComm*, 2018, **20**, 7170–7177.

21 Z. Iqbal and S. Veprek, *J. Phys. C Solid State Phys.*, 1982, **15**, 377–392.

22 I. H. Campbell and P. M. Fauchet, *Semiconductors*, 1986, **58**, 739–741.

23 C. Smit, R. A. C. M. M. Van Swaaij, H. Donker, A. M. H. N. Petit, W. M. M. Kessels and M. C. M. Van de Sanden, *J. Appl. Phys.*, 2003, **94**, 3582–3588.

24 S. Veprek, F.-A. Sarott and Z. Iqbal, *Phys. Rev. B*, 1987, **36**, 3344–3350.

25 J. C. Harmand, G. Patriarche, F. Glas, F. Panciera, I. Florea, J. L. Maurice, L. Travers and Y. Ollivier, *Phys. Rev. Lett.*, 2018, **121**, 1–5.

26 D. Tuschel, *Spectrosc. (Santa Monica)*, 2017, 32, 26–33.

27 P. W. Voorhees, *J. Stat. Phys.*, 1985, **38**, 231–252.

28 P. W. Voorhees, *Annu. Rev. Mater. Sci.*, 1992, **22**, 197–215.

29 A. Baldan, *J. Mater. Sci.*, 2002, **37**, 2379–2405.

30 Y. Hishikawa, N. Nakamura, S. Tsuda, S. Nakano, Y. Kishi and Y. Kuwano, *Jpn. J. Appl. Phys.*, 1991, **30**, 1008–1014.